CHEMISTRY OF MATERIALS

pubs.acs.org/cm

Article

Cooperative Interactions with Water Drive Hysteresis in a Hydrophilic Metal–Organic Framework

Published as part of Chemistry of Materials virtual special issue "C. N. R. Rao at 90".

Julius J. Oppenheim, Ching-Hwa Ho, Dalal Alezi, Justin L. Andrews, Tianyang Chen, Bhavish Dinakar, Francesco Paesani, and Mircea Dincă*

Cite This: *Chem. Mater.* 2024, 36, 3395–3404

Read Online

ACCESS | Metrics & More | Article Recommendations | Supporting Information

ABSTRACT: Devices that utilize the reversible capture of water vapor provide solutions to water insecurity, increasing energy demand, and sustainability. In all of these applications, it is important to minimize water adsorption–desorption hysteresis. Hysteresis is particularly difficult to avoid for sorbents that bind water strongly, such as those that take up below 10% relative humidity (RH). Even though the theoretical factors that affect hysteresis are understood, understanding the structure–function correlations that dictate the hysteretic behavior in water sorbents remains a challenge. Herein, we synthesize a new hexagonal microporous framework, Ni_2Cl_2BBTQ (H_2BBTQ = 2*H*,6*H*-benzo[1,2-*d*][4,5-*d*′]bistriazolequinone), to elucidate these principles. Uniquely among its known isoreticular analogues, Ni_2Cl_2BBTQ presents unusually high hysteresis caused by strong wetting seeded by a particularly strong zero-coverage interaction with water. A combination of vibrational spectroscopies and detailed molecular dynamics simulations reveals that this hysteretic behavior is the result of an intricate hydrogen-bonding network, in which the monolayer consists of water simultaneously binding to open nickel sites and hydrogen bonding to quinone sites. This latter hydrogen-bonding interaction does not exist in other isoreticular analogues: it prevents facile water dynamics and drives hysteresis. Our results highlight an important design criterion for water sorbents: in order to drive water uptake in progressively dry conditions, the common strategy of increasing hydrophilicity can cause strong wetting and the formation of superclusters, which lead to undesirable hysteresis. Instead, hysteresis-free water uptake at extremely low humidity is best promoted by decreasing the pore size, rather than increasing hydrophilicity.

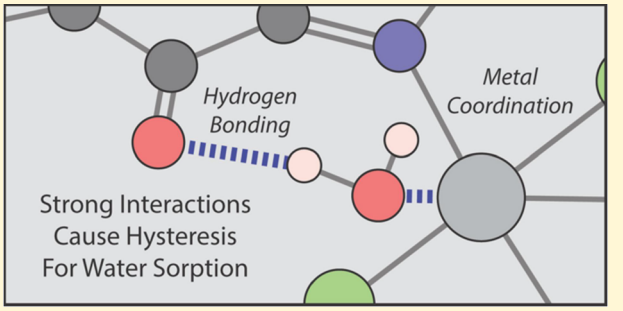

INTRODUCTION

The capture and control of water vapor is critical for several applications including desiccation, thermal battery heat storage, heat pump energy transfer, humidity control, desalination, and atmospheric water capture.[1,2] Metal–organic frameworks (MOFs) have been proposed as promising sorbents for the reversible binding of water due to their high porosity, water stability, crystallinity, and chemical tunability. However, the exact relationship between the chemical composition and the behavior of water within pores remains ambiguous. With clear structure–function principles, it will be possible to simultaneously optimize the working capacity, relative humidity for the onset of pore condensation, slope of isotherm, water cycling hysteresis, kinetics of sorption, water cycling stability, and isosteric enthalpy for the adsorption of water. These physical parameters dictate the utility of the sorbent for the desired applications.[1]

Many systematic studies have been performed to elucidate structure–function correlations, with a dominant focus on controlling the onset of pore condensation, increasing working capacity, and increasing water stability.[3−7] In order to more easily determine these correlations, there has been interest in developing the chemistry of materials based on bistriazolylarene ligands such as H_2BTDD = bistriazolodibenzodioxin, H_2BBTA = benzenebistriazole, and H_2bibta = bibenzotriazole. This family serves as an ideal model system due to exceptional hydrolytic stability derived from the kinetically inert late transition-metal–triazolate bonds.[8] The effects of isoreticular modification of pore size,[9] modification of the element in open metal sites,[10,11] modification of structural anion identity,[6] and the effect of pore shape[12] have been correlated with changes in the onset of pore condensation and working capacity.[11] Critically, the structure–function correlations determining

Received: January 20, 2024
Revised: March 8, 2024
Accepted: March 11, 2024
Published: March 26, 2024

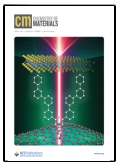

the presence and size of hysteretic loops have not yet been fully delineated. Even though there is an understanding of the maximum pore size before the onset of capillary condensation-driven hysteresis, the relationship between structure and water supercluster-based hysteresis is still unclear. Herein, we utilize this isoreticular platform to investigate the relationship between the framework structure and adsorption−desorption hysteresis, specifically the relationship between the cooperative binding of water, caused by simultaneous interactions with the nickel site and quinone sites, and the thermodynamics for formation of strong wetting films/water superclusters.

We report a metal−organic framework, Ni_2Cl_2BBTQ (H_2BBTQ = 2*H*,6*H*-benzo[1,2-*d*][4,5-*d*′]bistriazolequinone). This framework adopts a hexagonal topology, isoreticular to the previously described M_2X_2BBTA and M_2X_2BTDD frameworks. Due to the presence of the quinone functional group, the pores are more hydrophilic and bind water tightly. The structure of the hydrogen-bonding network is probed by a combination of variable humidity or variable temperature infrared and Raman spectroscopy, powder X-ray diffraction, and gravimetric analysis with detailed molecular dynamics simulations. We find that the quinone functional groups facilitate the binding of water below 0.5% relative humidity (RH) (at 25 °C) as a result of the cooperative binding of water to the open nickel site, concomitant with hydrogen bonding to the quinone groups. The framework has sluggish activation kinetics below 200 °C under high vacuum due to extreme hysteresis, leading to a reduction of the working capacity during 0−25% RH cycling at 25 °C with 2 h cycles from an ideal ∼0.20 to 0.11 g/g.

RESULTS AND DISCUSSION

Synthetic and Structural Details. Previous syntheses of nonporous MOFs using benzobistriazolequinone ($BBTQ^{2-}$) have utilized the conjugate base under aqueous hydrothermal conditions.[13,14] We hypothesized that conditions mimicking those used in the synthesis of isoreticular Ni_2Cl_2BBTA, which utilize a neutral ligand in an organic solvent, would prevent the formation of metal−ketone coordination bonds and form the desired hexagonal phase (Figure 1). Reaction of H_2BBTQ with $NiCl_2$ in acidic *N*,*N*-dimethylformamide gives rise to a crystalline, turquoise-colored material with the desired structure type. The crystal structure of the framework was refined against a synchrotron powder X-ray diffraction pattern in space group $R\bar{3}m$ with $a = b = 24.65$ Å and $c = 8.12$ Å (Figures S4.1 and 1b). The diameter of the maximally included sphere is 10.7 Å. The oxygen of water bound to the nickel center is crystallographically resolvable, though all other waters in the pores are disordered.

MOF Activation. Due to the narrow and hydrophilic pores that facilitate pore condensation, Ni_2Cl_2BBTQ is difficult to be activated under dynamic vacuum (3 μmHg) at 135 °C, the activation conditions used for Ni_2Cl_2BBTA, where water desorption is kinetically limited. After 12 h of activation under these conditions, the N_2 isotherm displays type I behavior, with a measured BET surface area of 704 m^2/g and a pore volume of 0.29 cm^3/g. After 36 h of activation, the surface area increases to 1146 m^2/g, with the corresponding pore volume of 0.45 cm^3/g (Figure S6.1).

To improve the rate of activation, higher temperatures are used. Thermogravimetric analysis of Ni_2Cl_2BBTQ (measured under a dry nitrogen flow with 1 °C/min heating) reveals a substantial mass loss between 160 and 200 °C, corresponding

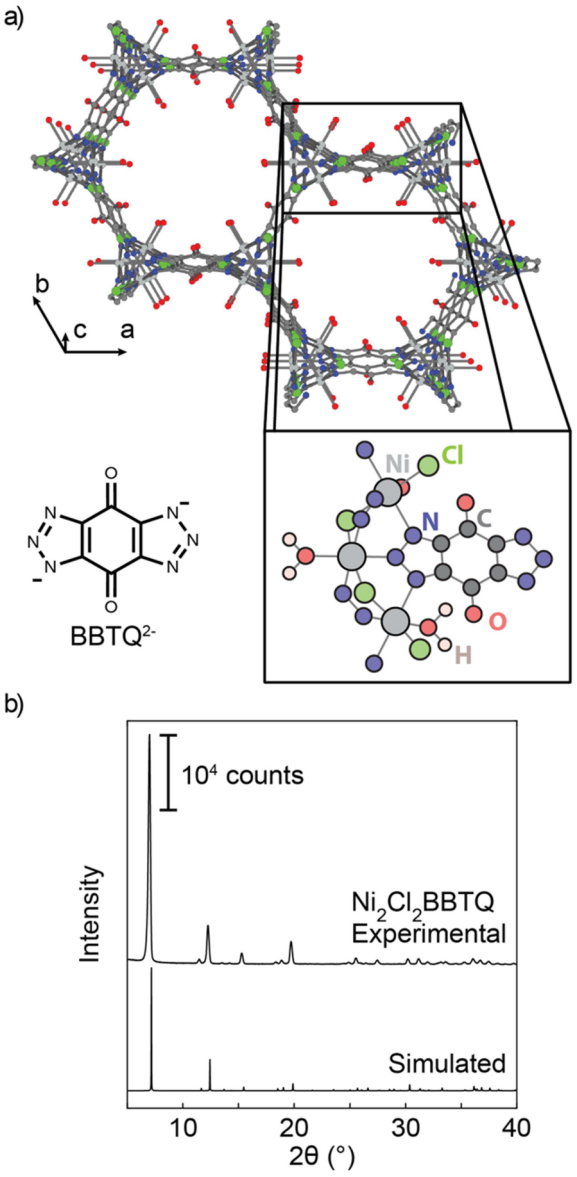

Figure 1. (a) Portion of the structure of Ni_2Cl_2BBTQ (with the central pore guest water molecules excluded). (b) Powder X-ray diffractogram of Ni_2Cl_2BBTQ (Cu Kα radiation).

to the removal of approximately four water molecules per nickel site (Figure 2c). To confirm the stability of the material at these elevated temperatures, we performed variable-temperature powder X-ray diffraction. Upon heating to 250 °C, we observe the preservation of crystallinity, with an associated small irreversible decrease in the unit cell volume from ∼4200 to ∼4000 $Å^3$, consistent with the cell contraction upon solvent loss (Figure 2a).

Upon activation of the material under dynamic vacuum at 200 °C for 12 h, the material again displays a type I N_2 isotherm, with an increased BET surface area of 1258 m^2/g and a pore volume of 0.50 cm^3/g (Figure 2b). This measured surface area lies between the theoretical surface area for a model structure with no waters in the pores, at 1363 m^2/g, and a model structure with one water bound to each nickel site, at 1,218 m^2/g, suggesting that even heating at 200 °C for 12 h does not result in complete activation of the framework.

https://doi.org/10.1021/acs.chemmater.4c00172
Chem. Mater. 2024, 36, 3395−3404

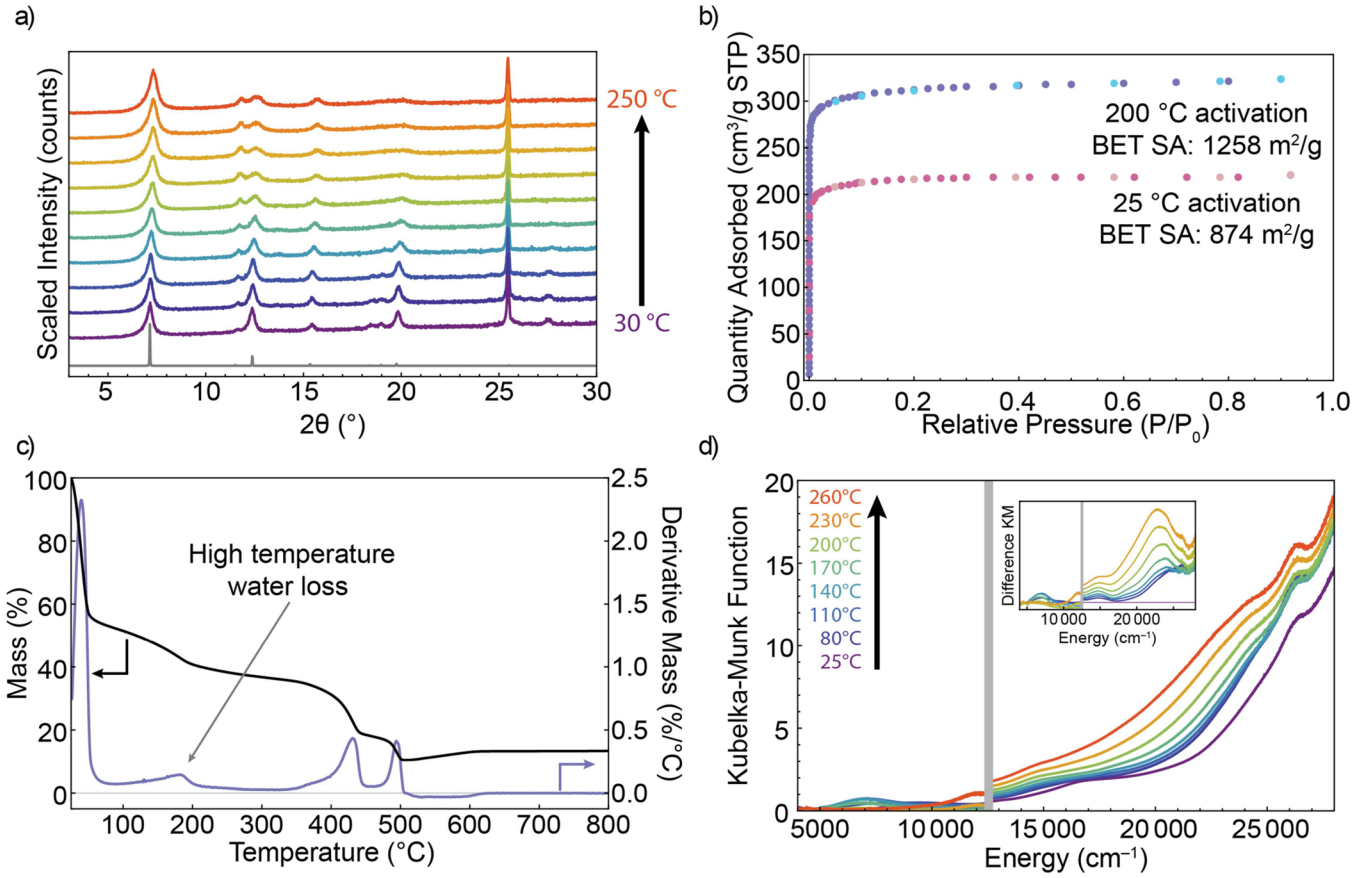

Figure 2. (a) Variable-temperature powder X-ray diffractogram (Cu Kα radiation). The gray trace is a simulated pattern. The reflection at 25.5° corresponds to the Al_2O_3 sample holder. (b) N_2 isotherms of Ni_2Cl_2BBTQ activated at 25 and 200 °C. (c) Thermogravimetric analysis for Ni_2Cl_2BBTQ. (d) Variable-temperature UV−vis−NIR spectra of Ni_2Cl_2BBTQ.

Upon activation of the framework at 200 °C, an irreversible chemical change occurs, characterized by a darkening in color, proceeding from green to purple to black. Variable-temperature ultraviolet−visible−near-infrared spectroscopy (under a flow of helium gas) reveals the appearance of two new absorption bands at 14,877 and 22,857 cm^{-1} (672 and 438 nm) upon heating, with the onset temperature below 80 °C (Figure 2d). We attribute these changes to the reduction of quinone to hydroquinone via water oxidation, where there is an equilibrium between quinone and hydroquinone with quinhydrone (i.e., quinone−hydroquinone dimer). These bands correspond to the quinhydrone charge-transfer excitation and hydroquinone $\pi-\pi^*$ excitation, respectively.[15] It is difficult to quantify precisely the ratio of quinone to hydroquinone as the equilibrium constant between quinone−hydroquinone and quinhydrone is not known, and ^{13}C-ssNMR spectra do not exhibit any features (likely due to paramagnetic broadening by spin polarization from the nickel sites). However, given that the quinhydrone band grows monotonically with temperature, we expect that the quinone content outnumbers hydroquinone (ideally at an equal quinone−hydroquinone content, the quinhydrone band would reach a maximum and decrease in intensity after hydroquinone exceeds quinone content).

The carbon 1s region of X-ray photoelectron spectra corroborate the assignment for partial reduction of quinone to hydroquinone. A spectrum of pristine material displays a small band at 288 eV and a larger band at 286 eV, corresponding to the C═O and C−N carbons, respectively (Figure S7.1). Upon activation, the relative intensity of the 288 eV band to the 286 eV band decreases, consistent with the reduction of quinone, as an aromatic alcohol also appears at around 286 eV. Additionally, the spectrum of the material that was cycled through many water isotherms and activated several times displays a weaker $\pi-\pi^*$ satellite band at 291 eV compared with the pristine Ni_2Cl_2BBTQ, consistent with the increasing amount of hydroquinone.

There is a slight decrease in the ratio of chloride/nickel from 1.0 to 0.77, as measured by X-ray photoelectron spectroscopy, which occurs only during the initial activation of the framework (Figures S7.3 and S7.4). The slight loss of chloride is attributed to the exchange of chloride to hydroxide, concomitant with the formation of hydrochloric acid, since there is no evidence of the reduction of nickel by X-ray photoelectron spectroscopy. Given that X-ray photoelectron spectroscopy is a surface technique, this reactivity pattern may be considered as surface passivation that occurs during the first activation.

Water Sorption. The water isotherms of Ni_2Cl_2BBTQ display type I behavior, consistent with the water isotherm of a microporous framework (Figure 3a).[16] The maximum capacity of the framework after activation at 200 °C is 0.38 g/g (approximately four water molecules per nickel site). At 9.6% RH, the quantity of water adsorbed is 0.22 g/g, indicating that Ni_2Cl_2BBTQ adsorbs most of its maximal water uptake at extremely low relative humidity. The onset for pore condensation is consistent with other smaller pore frameworks, such as the isoreticular Ni_2Cl_2BBTA. There is a slight positive

https://doi.org/10.1021/acs.chemmater.4c00172
Chem. Mater. 2024, 36, 3395−3404

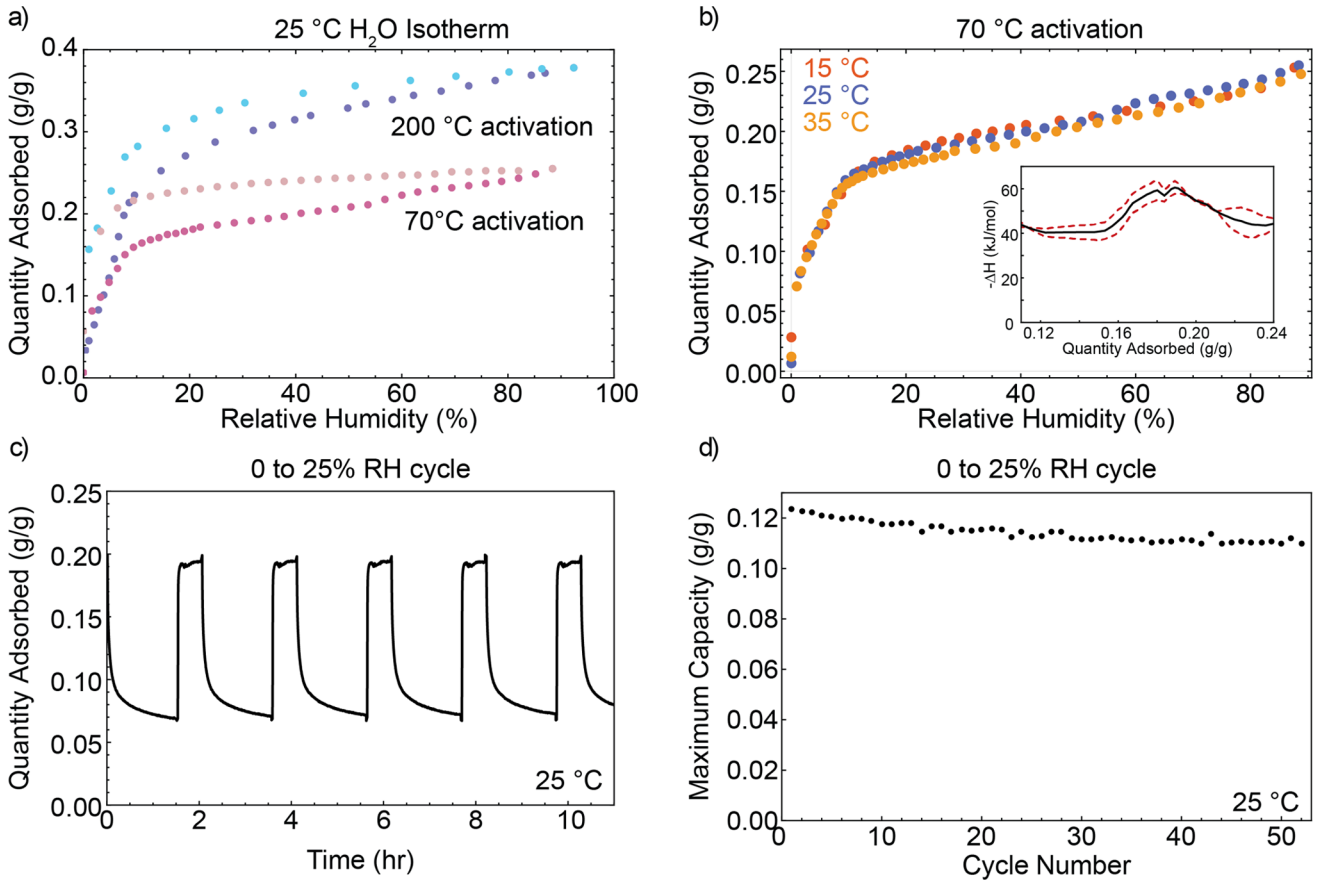

Figure 3. (a) Water isotherm of Ni_2Cl_2BBTQ with activation at 200 and 70 °C. (b) Variable-temperature water isotherm of Ni_2Cl_2BBTQ and the isosteric enthalpy of adsorption (dashed lines denote standard error). (c) Cycling at 25 °C between 0 and 8 mbar. (d) Working capacity during cycling over 52 cycles.

slope at a higher relative humidity, which we attribute to water condensation on the exterior of and in between crystallites.[17]

The high temperatures and extended activation times required to maximize the N_2 surface area are consistent with the expectation of a large hysteresis in the water isotherm. Kinetically hindered desorption may be caused by a large barrier for dissociating water due to the strong hydrogen-bonding network (this can be considered as a water supercluster or as thick pore wetting occurring prior to capillary condensation).[18,19] Indeed, upon desorption to 25 °C and 1.0% RH, there is still 0.16 g/g of adsorbed. This contrasts with the water isotherms for Ni_2Cl_2BBTA, which displays minimal hysteresis despite adsorbing water at lower RH.[9] The nature of the hysteresis with Ni_2Cl_2BBTQ differs from traditional ones, such as capillary condensation that occurs in frameworks with pores larger than 20 Å, or hysteresis caused by flexible pores that undergo expansion and contraction.[2]

Variable-temperature isotherms measured at 15, 25, and 35 °C were analyzed in order to measure the isosteric enthalpy of adsorption for water (Figure 3b). For this measurement, the sample was reactivated at 70 °C under dynamic vacuum (70 °C being chosen over 200 °C in order to prevent the possibility of slight framework degradation from affecting the calculation). The three isotherms display a similar uptake. The isosteric enthalpy of adsorption was calculated using linear interpolation, as none of the typical sorption models fit well to the data. It was not interpolated below 6 mmol/g due to insufficient data at very low RH. The isosteric enthalpy of adsorption was calculated to be roughly between 40 and 60 kJ/mol, consistent with the isosteric enthalpy of adsorption of water in similar microporous MOFs.[1] This value is higher than the enthalpy of vaporization for pure water at 40.7 kJ/mol, consistent with strong binding in the pore under confinement.[20] Given that this measurement was performed with activations at low temperature, it is difficult to experimentally bound the isosteric enthalpy of adsorption for the monolayer of water.

To test the stability of the framework for use as an adsorbent, cycling experiments were performed. In particular, the framework was cycled between 0 and 25.2% RH at 25 °C with 30 min for adsorption and 90 min for desorption. Whereas the kinetics of adsorption are fast (<5 min), the desorption process is slow: complete desaturation does not occur even after 1 h at 0% RH. The working capacity for 2 h adsorption−desorption cycles decreases by 11% over 52 cycles, with a mean working capacity of 0.11 g/g (Figures 3c,d and S8.1). We attribute the slight decrease to a combination of reduction of the quinone to hydroquinone during desorption, the small amount of chloride to hydroxide exchange, and any potential framework collapse that may occur as a result of the large internal forces the material undergoes during cycling. Importantly, the hysteresis is not responsible for the loss in working capacity: the isoreticular and nonhysteretic Ni_2Cl_2BBTA loses 8% of its capacity during temperature swing cycling, although the mechanism of capacity loss need not be the same.[9]

https://doi.org/10.1021/acs.chemmater.4c00172
Chem. Mater. 2024, 36, 3395−3404

The cause of the sluggish desorption kinetics differs from that for typical materials, whose kinetics are limited by external diffusion. For a typical nonhysteretic sorbent during cycling, the rate of sorption is most significantly modified by the shape of the isotherm (which dictates the RH gradient between the sorbent bed and atmosphere), rather than by the intrinsic rate constant.[21] However, for Ni_2Cl_2BBTQ, the intrinsic rate of desorption is quite slow (even on the time scales for isothermal measurements), and we expect that the cycling is internally kinetics/diffusion limited. Certainly, this is not ideal for a practical sorbent, and identifying the physical property that causes such slow desorption is necessary such that it can be avoided for other sorbents.

Thermodynamics of Water Adsorption by Molecular Dynamics Simulation. To further probe the interaction between the framework and water at the lowest coverage, detailed molecular dynamics (MD) simulations were performed using the MB-pol many-body potential (details in Supplemental Section 1).[22−24] As the water loading increases from 0.056 to 3.0 mol H_2O/mol Ni, the adsorption enthalpy increases sharply from −15.3 to approximately −13.3 kcal/mol (−64 to −56 kJ/mol), and subsequently remains relatively constant (Figure 4a). This sharp increase in the adsorption enthalpy corresponds to the pore condensation step below 5% RH.

At the lowest loading (only one water molecule loaded within the framework), the most probable distance between the open nickel site and the oxygen atom in water is approximately 2.0 Å, as illustrated in the radial distribution function (RDF, Figure S10.1). This observation suggests that the nickel sites predominantly serve as the primary sites for the initial hydration and water capture. However, rigid coordinate scans indicate that the interaction energy between water and the open nickel site is only −8 kcal/mol, significantly smaller than the zero-coverage adsorption enthalpy of −15.3 kcal/mol (Figure S9.3). This suggests that the interaction energy between water and quinone also exerts a significant influence on adsorption. This secondary interaction is further indicated by the RDF between the quinone oxygen and water hydrogen, with a most probable distance of approximately 1.9 Å. (Figure S10.1). This pair of key interactions that leads to strong water uptake at the monolayer level is illustrated in Figure 4c.

The entropy of water exhibits a trend similar to the adsorption enthalpy as a function of the water loading (Figure 4b). It displays a rapid increase from 14.8 to 17.6 cal/mol K as the loading increases from 0.056 to 1.2 mol of H_2O/mol of Ni, followed by a gradual decrease to 17.0 cal/mol K when the loading is further increased to 3.0 mol of H_2O/mol of Ni, which is attributed to the increasing complexity of the hydrogen-bond network. Remarkably, this behavior diverges from that observed for NU-1500-Cr (a framework previously studied by the same methods), in which the entropy rapidly decreases during capillary condensation.[25] This difference can be ascribed to the characteristics of the primary interaction sites during the initial hydration phase, resulting in distinct dynamic properties of water molecules, which will be further elaborated in the subsequent section.

While the entropy trend of water in Ni_2Cl_2BBTQ differs from that in NU-1500-Cr, both cases exhibit notable variations in adsorption enthalpy and entropy around the adsorption step on the isotherm, which correspond to filling the regions with the largest void space within the two frameworks. This observation offers a characteristic feature that can be employed

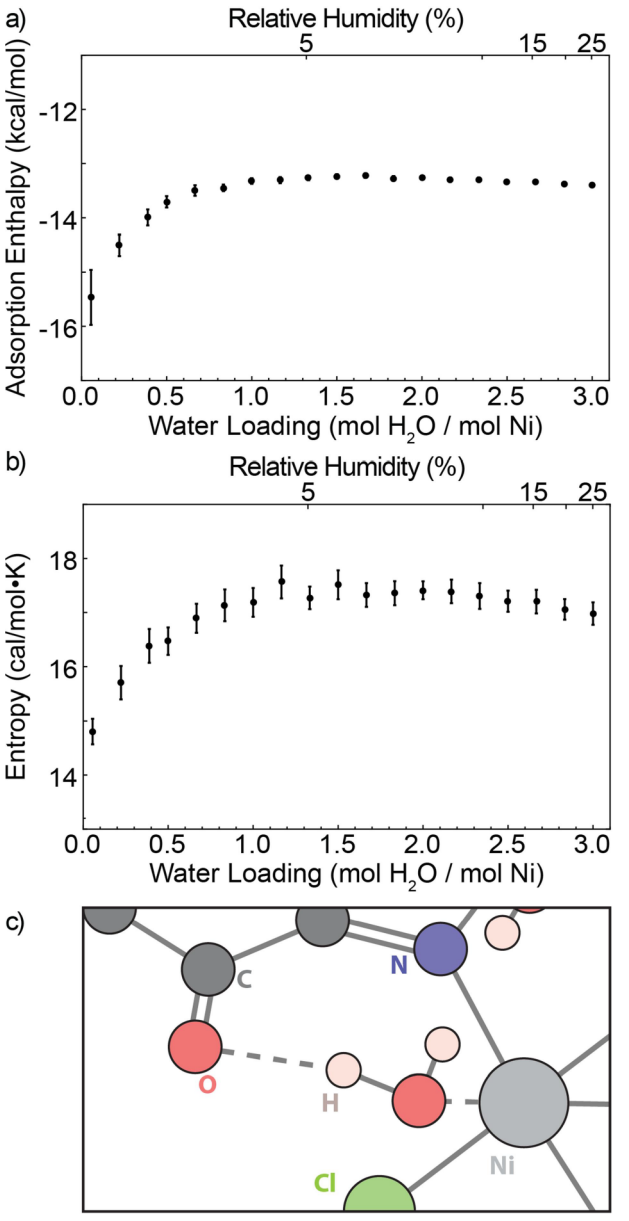

Figure 4. Thermodynamic properties of water within Ni_2Cl_2BBTQ at different loadings. (a) The adsorption enthalpy and (b) water entropy. (c) A representative structure from molecular dynamics simulations in which a water molecule is simultaneously bound to the nickel site and hydrogen bonds to the quinone site.

in MD simulations to determine the relative humidity value corresponding to the adsorption step and characterize the pore filling mechanism within a given framework structure.

Dynamical Properties of Water Adsorption. To shed light on the difference in the water entropy at the early stage of hydration, several dynamical properties of water at different loadings were calculated by using MD simulations. The spatial distribution of water within the pores were calculated as a function of water loading (Figure 5a, defining nickel site occupation within 2.5 Å and quinone site occupation within 2.2 Å). Strong correlations between nickel and quinone site occupation suggest that water binding to open nickel sites is always accompanied by hydrogen bonding to the quinone oxygen, which notably contributes to the adsorption enthalpy at the early stage of hydration, as shown in Figure 4a. The

https://doi.org/10.1021/acs.chemmater.4c00172
Chem. Mater. 2024, 36, 3395−3404

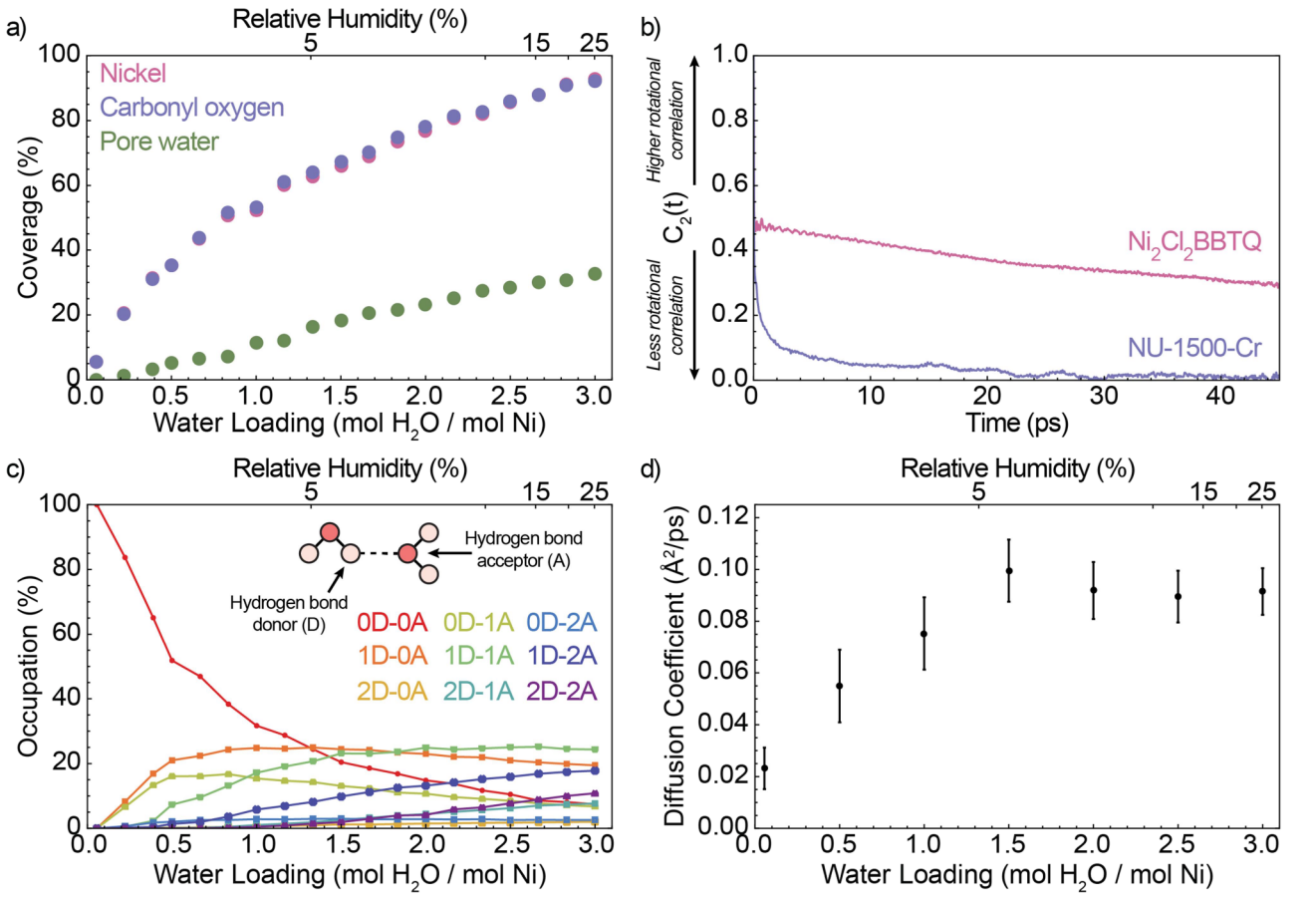

Figure 5. Dynamical properties of water within Ni_2Cl_2BBTQ. (a) Percentage of occupancy of Ni, carbonyl oxygen, and the center of the pore at different water loadings. (b) Orientational correlation function of a single water molecule confined in Ni_2Cl_2BBTQ (red). For comparison, the corresponding orientational correlation function confined in NU-1500-Cr (blue) calculated from ref 25 is shown. (c) Hydrogen-bond topologies of water and (d) diffusion coefficients of water along the pore direction at different loadings.

confinement effects of Ni_2Cl_2BBTQ are further elucidated by comparing the orientational correlation function of a single water molecule within Ni_2Cl_2BBTQ with that of the previously studied and larger-pore NU-1500-Cr (Figure 5b). We find that the reorientation rate of water in Ni_2Cl_2BBTQ is slower than that in NU-1500-Cr. This suggests that Ni_2Cl_2BBTQ imposes stronger constraints on the motion of a water molecule than does the chromium MOF, as the water molecule binds to the respective primary interaction sites in the initial hydration stage. With Ni_2Cl_2BBTQ, a water molecule binds to a single Ni site, and its rotation is constrained by hydrogen bonding to the nearby quinone. In contrast, for NU-1500-Cr, the first water molecules bind exclusively to Cr sites during the initial hydration stage and are overall less constrained than those in Ni_2Cl_2BBTQ. As a result, the different entropic behavior of water at low loadings between the two MOFs: increasing with RH for Ni_2Cl_2BBTQ, and decreasing for NU-1500-Cr, directly correlates with the constraint imposed on water molecules particularly by the neighboring quinone sites in the former.

Analysis of the statistics of water molecules located near the center of the pore in Ni_2Cl_2BBTQ provides further insight into the confinement effects (Figure 5a). Notably, only ~50% of the nickel sites are saturated with water upon loading of 1 mol H_2O/mol Ni. Even at the highest loading considered here, 3 H_2O/mol Ni, approximately 8% of the nickel sites remain unsaturated. At this highest loading, the remainder of the water that could be occupying the unsaturated nickel sites instead lies within the center of the pore. The water occupation at the central pore positions exhibits a seemingly linear growth with increasing water loading. As the pore water occupation increases, the hydrogen-bonding network becomes more connected (Figure 5c) with a distribution of water having multiple donor (D) or acceptor (A) partners. Consequently, as the water loading increases, the energy difference between saturating a nickel site and participating in the hydrogen-bonding network gradually diminishes. This suggests that entropic effects gradually become the main factor determining the percentage of Ni sites being saturated at a high water loading.

The confinement effects of Ni_2Cl_2BBTQ on water molecules are further reflected in the translational transport properties. The diffusion coefficient of water molecules along the pore direction (crystallographic *c*-direction) increases with the water loading (Figure 5d). This is consistent with a large population of water immobilized by nickel and quinone sites at low water loading, resulting in pronounced hindrance to water translational mobility. At higher water loading, there is a corresponding rise in the percentage of water molecules situated near the center of the pore, which reduces the constraints on translational mobility. A similar trend in diffusion coefficients at varying water loadings has been observed in other systems, such as Zn(l-L)Cl[26] and Co-MOF-74,[27] and has been suggested in the investigation of water in isoreticular Co_2Cl_2BTDD.[28] The analogous trend in

https://doi.org/10.1021/acs.chemmater.4c00172
Chem. Mater. 2024, 36, 3395−3404

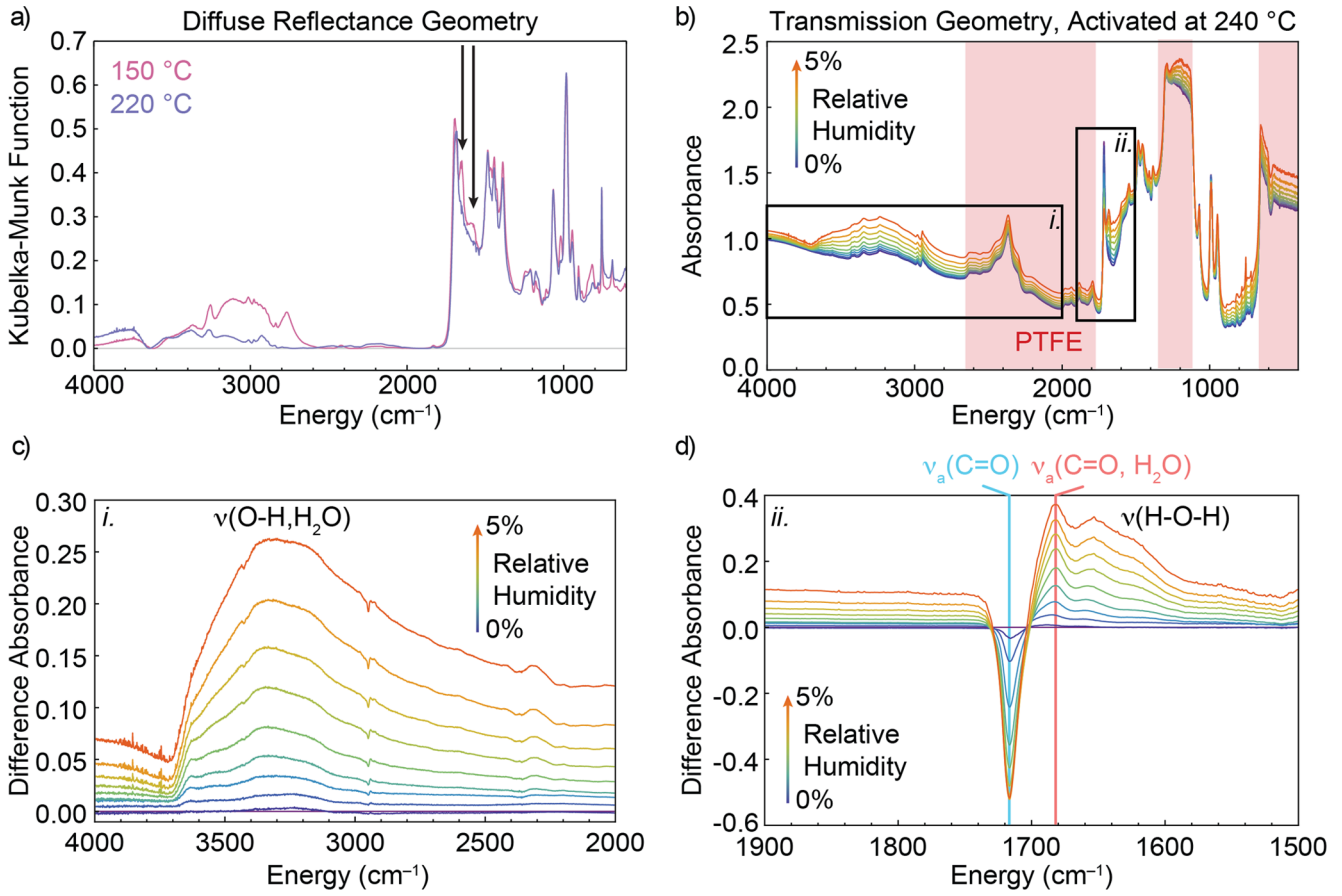

Figure 6. (a) DRIFT spectra of Ni_2Cl_2BBTQ upon activation at 150 and 220 °C. (b) Absorbance spectra upon dosing from 0 to 5% RH. Red areas highlight the vibrational modes of polytetrafluoroethylene. (c) Difference absorbance spectra of the water region. (d) Difference absorbance spectra of the quinone region.

diffusion coefficients observed in these MOFs can be attributed to their similarity in strong interactions with the framework at low water loadings, where most water molecules either saturate the metal sites or establish hydrogen bonds with the framework.

Vibrational Spectroscopic Characterization. Vibrational spectroscopy supports the structural assignments of confined water from MD simulations. Specifically, the symmetric and antisymmetric ν(C═O) quinoidal vibrational modes were used as spectroscopic handles to probe the water–MOF interaction. The shifts in these vibrational bands upon coordination to water directly report the spatial distribution of water as a function of RH. In situ infrared (IR) spectroscopy was performed under a controlled RH between 0.2 and 26% in both diffuse reflectance infrared Fourier transform spectroscopy (DRIFTS) and transmission geometries.

Upon heating the sample to 150 °C under a dry argon stream, sharp vibrational bands are displayed from 2400 to 3600 cm^{-1}, consistent with a hydrogen-bonding network of pore-confined water. Upon activation at 220 °C, the bands at approximately 1610 and 1650 cm^{-1} disappear, while the band at 1700 cm^{-1} sharpens (Figure 6a). The intensity of the water bands also decreases, consistent with a more complete activation of the framework. Upon dosing the material to approximately 5% RH, the water bands and the bands at 1610 and 1650 cm^{-1} reappear (Figure S11.1). Above 5% RH, no further changes occur, indicating that the material was fully saturated with water. Upon reactivation of the material at 150 °C, the water bands around 3000 cm^{-1} as well as the 1610 and 1650 cm^{-1} bands decrease in intensity, indicating reversibility.

To determine the changes in the hydrogen-bonding network below 5% RH, we performed in situ IR spectroscopy in a transmission cell designed such that incremental quantities of water vapor could be dosed at known pressures. Upon activation of the framework at 240 °C, we observe a decrease in intensity of the bands between 1620 and 1660 cm^{-1}, as well as the conversion of a band from 1684 to 1716 cm^{-1}, with an isosbestic point near 1700 cm^{-1} (Figure S11.2). After activation, a few sharp bands in the water region remain, ranging from 2947 to 3558 cm^{-1}, consistent with the well-defined hydrogen-bond network of residual water in the pores, partial reduction of the quinone to hydroquinone, and/or a small amount of chloride-to-hydroxide anion exchange.

Two distinct features appear upon dosing with water up to 5% RH. First, a very broad band spanning from 3700 to approximately 2500 cm^{-1} increases in intensity. This band is associated with the ν(O–H) water vibrational modes. The broad features are diagnostic of a hydrogen-bond network that is not ordered. Second, there is a decrease in intensity for the band at 1716 cm^{-1} and an increase in intensity for both bands at 1684 and 1653 cm^{-1} (Figure 6b–d). The band at 1716 cm^{-1} is attributed to ν_{asym}(C═O), the frequency of the B_{1u} quinone stretching mode. In order to assign the 1684 and 1653 cm^{-1} bands, we repeated the experiment while dosing with D_2O. Isotopic labeling reduces the relative intensity of the 1653 cm^{-1} band (Figure S11.5), suggesting that it corresponds

https://doi.org/10.1021/acs.chemmater.4c00172
Chem. Mater. 2024, 36, 3395–3404

to the water bending mode, while the 1684 cm^{-1} corresponds to the ν_{asym}(C═O, H-bond) mode (the corresponding quinone stretching mode with hydrogen bonding to water). The assignment of ν_{asym}(C═O) and ν_{asym}(C═O, H-bond) to the 1716 and 1684 cm^{-1} bands is in agreement with the observed isosbestic point, which indicates an interconversion between the two species.

Given these spectral assignments, structural information as a function of the RH may be extracted. Integration of the difference spectra for a particular vibrational band as a function of RH reveals changes in the distribution of molecules in the system. Comparisons of the difference spectra for the regions comprising the O−H (integrated from 2975 to 4000 cm^{-1}) and the asymmetric C═O stretching mode (intensity determined by Gaussian deconvolution, Figure S11.3) reveal the RH values where water coordinates and then saturates the quinone groups (Figure 7a). The integrated difference spectra

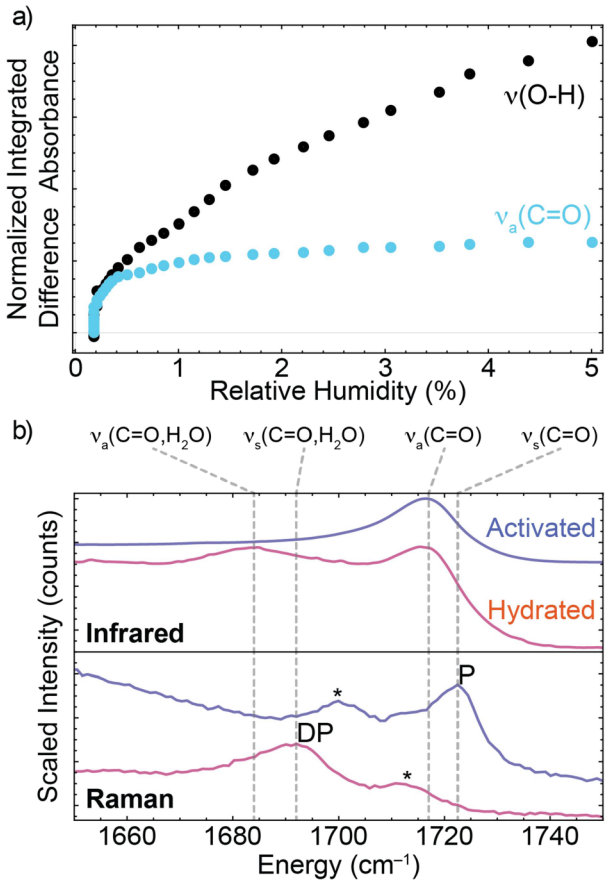

Figure 7. (a) Normalized integrated difference absorbance for the water ν(O−H) band and ν_{asym}(C═O) band. (b) Comparison of the IR and Raman spectra of activated and hydrated Ni_2Cl_2BBTQ. *Indicates an overtone, DP indicates a depolarized band, and P indicates a polarized band.

for the water band reveal a steep increase below 0.5% RH, followed by a slower increase in intensity up to 5% RH. For the quinone vibrational mode, the intensity decreases rapidly from 0 to 0.5% RH, reaching a plateau around 1.5% RH. The similar behavior of the integrated difference spectra below 0.5% RH suggests that the first water that enters the pores coordinates to the quinone, and the quinone groups are saturated with water before reaching 1.5% RH, in agreement with the predictions from MD simulations.

To probe the local structure of water around the quinones, we measured the depolarization ratios of the quinone symmetric vibrations using Raman spectroscopy (excitation wavelength of 785 nm) for the unactivated and activated Ni_2Cl_2BBTQ. The Raman spectrum of the unactivated framework displays bands at 1692 and 1712 cm^{-1}, whereas the spectrum of the activated framework displays bands at 1701 and 1723 cm^{-1}. The bands at 1712 and 1701 cm^{-1} in the unactivated and activated spectra are likely overtones, as they lie at approximately 2 times the energy of other observed bands, 855 and 852 cm^{-1}, respectively (with slight deviations likely due to anharmonicity). We can, therefore, attribute the band at 1723 cm^{-1} to the symmetric quinone vibrational mode ν_{sym}(C═O) and the band at 1692 cm^{-1} to the symmetric quinone vibrational mode where the quinone is hydrogen-bonding to water, ν_{sym}(C═O, H_2O) (Table 1).

Table 1. Assignment of the Quinone Vibrational Modes

ν(C═O)	antisymmetric, B_{1u}	symmetric, A_{1g} (depolarization ratio)
activated	1716 cm^{-1}	1723 cm^{-1} (0.60)
bound to water	1684 cm^{-1}	1692 cm^{-1} (0.74)

Given these assignments, we measured the depolarization ratio, ρ, whose value is a measure of the symmetry for a vibrational mode, to gain insights into the local structure of the second water layer (Figures 7b, S12.1, and S12.2). For BBTQ, a molecule with local D_{2h} symmetry, the depolarization ratio for an A_g symmetric vibrational mode should be between 0 and 0.75, while the ratio for a vibrational mode with any other symmetry will be 0.75.[29,30] We find that the symmetric ν_{sym}(C═O) band at 1723 cm^{-1} is a polarized band with ρ = 0.60, which is consistent with a totally symmetric vibrational mode. However, the symmetric ν_{sym}(C═O, H_2O) band at 1692 cm^{-1} is a depolarized band with ρ = 0.74, inconsistent with a totally symmetric vibrational mode. We attribute the depolarization to a breaking of symmetry at the quinone away from ideal D_{2h} symmetry due to strong coupling between the quinone vibrational mode and the water vibrational modes.

The assignments of quinone vibrational modes are consistent with the theoretical calculations. The nonscaled DFT-calculated vibrational modes of $BBTQ^{2-}$ and $2H_2O$·$BBTQ^{2-}$ are ν_{sym}(C═O) = 1688 cm^{-1}, ν_{asym}(C═O) = 1684 cm^{-1}, ν_{sym}(C═O, H_2O) = 1681 cm^{-1}, and ν_{asym}(C═O, H_2O) = 1672 cm^{-1} antisymmetric. Experimentally and computationally, the symmetric vibrational mode is 5−10 cm^{-1} higher in energy than the antisymmetric vibrational mode, and there is a red shift upon coordination to water, measured 32 cm^{-1} experimentally and calculated at 10 cm^{-1} by using DFT.

CONCLUSIONS

In summary, isoreticular modification of Ni_2Cl_2BBTA to the quinoidal Ni_2Cl_2BBTQ greatly increases the interaction strength of the framework with water, causing monolayer wetting and formation of superclusters, pore condensation at extremely low relative humidity, and strong adsorption−desorption hysteretic behavior. In particular, the strong interaction strength is due to the cooperative interaction between water binding at the unsaturated nickel site and concomitant binding at the quinone sites, allowing for the formation of a hydrogen-bond network at low RH. Application

https://doi.org/10.1021/acs.chemmater.4c00172
Chem. Mater. 2024, 36, 3395−3404

of this principle of multiple neighboring adsorption sites to larger pore frameworks may enable the design of frameworks with a high capacity and very low relative humidity onset for pore condensation, which may be useful in certain scenarios. Moreover, by designing sorbents that avoid multiple neighboring adsorption sites and instead achieve low RH adsorption through small pore sizes, hysteresis caused by strong wetting may be avoided.

EXPERIMENTAL SECTION

Materials. Hydrazine monohydrate (80.0 wt %, TCI America), acetic acid (ACS grade, Fisher Chemical), sodium nitrite (Alfa Aesar, 97% min), $NiCl_2{\cdot}6H_2O$ (Strem Chemicals), HCl (36.5−38%, VWR), methanol (VWR), and *N*,*N*-dimethylformamide (VWR, 99.9% min) were used as received.

Synthesis of Tetraamino-*p*-benzoquinone (TABQ). TABQ was synthesized according to the literature.[31] To a 500 mL round-bottom flask was added 35 g of TPBQ, followed by the addition of 125 mL of hydrazine hydrate (80.0 wt %). The reaction mixture was heated at 65 °C for 2 h, after which it was cooled to room temperature, filtered, and washed with DI water until the filtrate coming out is colorless. A deep purple crystalline solid was isolated. 13C-NMR (DMSO) δ 179.32, 121.84 ppm

Synthesis of 2*H*,6*H*-Benzo[1,2-*d*][4,5-*d*′]bistriazolequinone (H_2BBTQ). 1.182 g TABQ (1.182 g, 7.0 mmol, 1 equiv) was dissolved in 24 mL of acetic acid with stirring. A solution of 1.584 g $NaNO_2$ (23.0 mmol, 3.3 equiv) in 28 mL water was added dropwise over the course of 10 min to the TABQ solution. The mixture was stirred for 24 h. Solids were collected by vacuum filtration and washed three times with cold water. The solids were recrystallized by dissolving in boiling water and cooling in a fridge overnight. Gold/yellow crystals were collected by filtration. A second recrystallization was performed by dissolving the solids in 80 °C water and acidification with concentrated HCl until the pH = 1. The yellow/green crystals (0.633 g, 47% yield, 3.3 mmol), were collected by filtration. 13C-NMR (DMSO) δ 172.95, 146.46 ppm

Synthesis of Ni_2Cl_2BBTQ. 49.96 mg H_2BBTQ (0.26 mmol, 1 equiv) and 186.18 mg $NiCl_2{\cdot}6H_2O$ (0.78 mmol, 3.0 equiv) were dissolved in 20 mL of *N*,*N*-dimethylformamide and 21.9 μL concentrated HCl (0.26 mmol, 1.0 equiv). The solution was heated at 130 °C for 3 days. The solution was washed three times with *N*,*N*-dimethylformamide, two times with water, and two times with methanol (the solution was decanted and replaced each time). The blue/green solids were dried by activation at 100 °C (to form a free-flowing powder) or rigorously activated at 200 °C (to remove the majority of water from the pores). Elemental: $Ni_2Cl_2(C_6O_2N_6) \cdot 7\ H_2O$. (exp) C 15.50%, H 3.15%, N 16.39%. (meas) C 14.34%, H 2.81%, N 16.72%.

ASSOCIATED CONTENT

Supporting Information

The Supporting Information is available free of charge at https://pubs.acs.org/doi/10.1021/acs.chemmater.4c00172.

General information, synthetic methods, nuclear magnetic resonance spectroscopy, powder X-ray diffractometry, scanning electron microscopy, N_2 isotherms, X-ray photoelectron spectroscopy, water isotherms and cycling, force field parameters, radial distribution function of water, infrared spectroscopy, and Raman spectroscopy (PDF)

Crystallographic data of Ni_2Cl_2BBTQ (cif)

AUTHOR INFORMATION

Corresponding Author

Mircea Dincă − *Department of Chemistry, Massachusetts Institute of Technology, Cambridge, Massachusetts 02139, United States;* orcid.org/0000-0002-1262-1264; Email: mdinca@mit.edu

Authors

Julius J. Oppenheim − *Department of Chemistry, Massachusetts Institute of Technology, Cambridge, Massachusetts 02139, United States;* orcid.org/0000-0002-5988-0677

Ching-Hwa Ho − *Department of Chemistry and Biochemistry, University of California, San Diego, La Jolla, California 92037, United States;* orcid.org/0000-0002-3468-4311

Dalal Alezi − *Department of Chemistry, Faculty of Science, King Abdulaziz University, Jeddah 21589, Saudi Arabia;* orcid.org/0000-0002-3462-1193

Justin L. Andrews − *Department of Chemistry, Massachusetts Institute of Technology, Cambridge, Massachusetts 02139, United States*

Tianyang Chen − *Department of Chemistry, Massachusetts Institute of Technology, Cambridge, Massachusetts 02139, United States;* orcid.org/0000-0003-3142-8176

Bhavish Dinakar − *Department of Chemical Engineering, Massachusetts Institute of Technology, Cambridge, Massachusetts 02139, United States;* orcid.org/0000-0002-7611-101X

Francesco Paesani − *Department of Chemistry and Biochemistry and Materials Science and Engineering, University of California, San Diego, La Jolla, California 92037, United States; Halicioğlu Data Science Institute and San Diego Supercomputer Center, University of California, San Diego, La Jolla, California 92093, United States;* orcid.org/0000-0002-4451-1203

Complete contact information is available at: https://pubs.acs.org/10.1021/acs.chemmater.4c00172

Author Contributions

J.J.O.: investigation, methodology, visualization, and writing; C.-H.H.: investigation and writing; J.A.: investigation (supporting synthesis); D.A.: investigation (adsorption studies); T.C.: investigation (XPS); B.D.: investigation (infrared); F.P.: funding acquisition, supervision (theoretical and computational), and reviewing editing; and M.D.: funding acquisition, supervision, reviewing, and editing. All the authors discussed the results and commented on the manuscript. All authors have given approval to the final version of the manuscript. J.J.O. and C.-H.H. contributed equally to this work.

Funding

Work by the Dincă group was funded by the Brown Family Foundation. The computational component of this research was supported by the National Science Foundation through award no. 2311260. All simulations were carried out on Expanse at the San Diego Supercomputer Center (SDSC) through allocation CHE230052 from the Advanced Cyberinfrastructure Coordination Ecosystem: Services & Support (ACCESS) program, which is supported by NSF grants nos. 2138259, 2138286, 2138307, 2137603, and 2138296, as well as Triton Shared Computing Cluster (TSCC) at SDSC.

Notes

The authors declare no competing financial interest.

ACKNOWLEDGMENTS

We would like to thank Dr. Gang Liu for assistance in repairing instrumentation.

REFERENCES

(1) Liu, X.; Wang, X.; Kapteijn, F. Water and Metal−Organic Frameworks: From Interaction toward Utilization. *Chem. Rev.* **2020**, *120* (16), 8303−8377.

(2) Zhang, B.; Zhu, Z.; Wang, X.; Liu, X.; Kapteijn, F. Water Adsorption in MOFs: Structures and Applications. *Adv. Funct. Mater.* **2023**, No. 2304788.

(3) Lu, F.-F.; Gu, X.-W.; Wu, E.; Li, B.; Qian, G. Systematic Evaluation of Water Adsorption in Isoreticular UiO-Type Metal−Organic Frameworks. *J. Mater. Chem. A* **2023**, *11* (3), 1246−1255.

(4) Zheng, Z.; Hanikel, N.; Lyu, H.; Yaghi, O. M. Broadly Tunable Atmospheric Water Harvesting in Multivariate Metal−Organic Frameworks. *J. Am. Chem. Soc.* **2022**, *144* (49), 22669−22675.

(5) Hanikel, N.; Pei, X.; Chheda, S.; Lyu, H.; Jeong, W.; Sauer, J.; Gagliardi, L.; Yaghi, O. M. Evolution of Water Structures in Metal-Organic Frameworks for Improved Atmospheric Water Harvesting. *Science* **2021**, *374* (6566), 454−459.

(6) Rieth, A. J.; Wright, A. M.; Skorupskii, G.; Mancuso, J. L.; Hendon, C. H.; Dincă, M. Record-Setting Sorbents for Reversible Water Uptake by Systematic Anion Exchanges in Metal−Organic Frameworks. *J. Am. Chem. Soc.* **2019**, *141* (35), 13858−13866.

(7) Liu, L.; Telfer, S. G. Systematic Ligand Modulation Enhances the Moisture Stability and Gas Sorption Characteristics of Quaternary Metal−Organic Frameworks. *J. Am. Chem. Soc.* **2015**, *137* (11), 3901−3909.

(8) Rieth, A. J.; Wright, A. M.; Dincă, M. Kinetic Stability of Metal−Organic Frameworks for Corrosive and Coordinating Gas Capture. *Nat. Rev. Mater.* **2019**, *4* (11), 708−725.

(9) Rieth, A. J.; Wright, A. M.; Rao, S.; Kim, H.; LaPotin, A. D.; Wang, E. N.; Dincă, M. Tunable Metal−Organic Frameworks Enable High-Efficiency Cascaded Adsorption Heat Pumps. *J. Am. Chem. Soc.* **2018**, *140* (50), 17591−17596.

(10) Rieth, A. J.; Yang, S.; Wang, E. N.; Dincă, M. Record Atmospheric Fresh Water Capture and Heat Transfer with a Material Operating at the Water Uptake Reversibility Limit. *ACS central science* **2017**, *3* (6), 668−672.

(11) Wright, A. M.; Rieth, A. J.; Yang, S.; Wang, E. N.; Dincă, M. Precise Control of Pore Hydrophilicity Enabled by Post-Synthetic Cation Exchange in Metal−Organic Frameworks. *Chem. Sci.* **2018**, *9* (15), 3856−3859.

(12) Alezi, D.; Oppenheim, J. J.; Sarver, P. J.; Iliescu, A.; Dinakar, B.; Dincă, M. Tunable Low−Relative Humidity and High−Capacity Water Adsorption in a Bibenzotriazole Metal−Organic Framework. *J. Am. Chem. Soc.* **2023**, *145*, 25233.

(13) Bunzen, H.; Grzywa, M.; Aljohani, R.; Krug von Nidda, H.-A.; Volkmer, D. Synthesis, Thermal Stability, and Magnetic Properties of a Manganese(II) Coordination Framework Containing Bistriazolate Ligands. *Eur. J. Inorg. Chem.* **2019**, *2019* (41), 4471−4476.

(14) Bunzen, H.; Javed, A.; Klawinski, D.; Lamp, A.; Grzywa, M.; Kalytta-Mewes, A.; Tiemann, M.; von Nidda, H.-A. K.; Wagner, T.; Volkmer, D. Anisotropic Water-Mediated Proton Conductivity in Large Iron(II) Metal−Organic Framework Single Crystals for Proton-Exchange Membrane Fuel Cells. *ACS Appl. Nano Mater.* **2019**, *2* (1), 291−298.

(15) Tong, L.; Chen, Q.; Wong, A. A.; Gómez-Bombarelli, R.; Aspuru-Guzik, A.; Gordon, R. G.; Aziz, M. J. UV-Vis Spectrophotometry of Quinone Flow Battery Electrolyte for in Situ Monitoring and Improved Electrochemical Modeling of Potential and Quinhydrone Formation. *Phys. Chem. Chem. Phys.* **2017**, *19* (47), 31684−31691.

(16) Thommes, M.; Kaneko, K.; Neimark, A. V.; Olivier, J. P.; Rodriguez-Reinoso, F.; Rouquerol, J.; Sing, K. S. Physisorption of Gases, with Special Reference to the Evaluation of Surface Area and Pore Size Distribution (IUPAC Technical Report). *Pure and applied chemistry* **2015**, *87* (9−10), 1051−1069.

(17) Fuchs, A.; Knechtel, F.; Wang, H.; Ji, Z.; Wuttke, S.; Yaghi, O. M.; Ploetz, E. Water Harvesting at the Single-Crystal Level. *J. Am. Chem. Soc.* **2023**, *145* (26), 14324−14334.

(18) AbdulHalim, R. G.; Bhatt, P. M.; Belmabkhout, Y.; Shkurenko, A.; Adil, K.; Barbour, L. J.; Eddaoudi, M. A Fine-Tuned Metal−Organic Framework for Autonomous Indoor Moisture Control. *J. Am. Chem. Soc.* **2017**, *139* (31), 10715−10722.

(19) Towsif Abtab, S. M.; Alezi, D.; Bhatt, P. M.; Shkurenko, A.; Belmabkhout, Y.; Aggarwal, H.; Weseliński, Ł. J.; Alsadun, N.; Samin, U.; Hedhili, M. N.; Eddaoudi, M. Reticular Chemistry in Action: A Hydrolytically Stable MOF Capturing Twice Its Weight in Adsorbed Water. *Chem.* **2018**, *4* (1), 94−105.

(20) Beaton, C. *Heat Exchanger Design Handbook*; Hemisphere Publishing Corp, 1986.

(21) Bezrukov, A. A.; O'Hearn, D. J.; Gascón-Pérez, V.; Darwish, S.; Kumar, A.; Sanda, S.; Kumar, N.; Francis, K.; Zaworotko, M. J. Metal-Organic Frameworks as Regeneration Optimized Sorbents for Atmospheric Water Harvesting. *Cell Reports Physical Science* **2023**, *4* (2), No. 101252.

(22) Babin, V.; Leforestier, C.; Paesani, F. Development of a "First Principles" Water Potential with Flexible Monomers: Dimer Potential Energy Surface, VRT Spectrum, and Second Virial Coefficient. *J. Chem. Theory Comput.* **2013**, *9* (12), 5395−5403.

(23) Babin, V.; Medders, G. R.; Paesani, F. Development of a "First Principles" Water Potential with Flexible Monomers. II: Trimer Potential Energy Surface, Third Virial Coefficient, and Small Clusters. *J. Chem. Theory Comput.* **2014**, *10* (4), 1599−1607.

(24) Medders, G. R.; Babin, V.; Paesani, F. Development of a "First-Principles" Water Potential with Flexible Monomers. III. Liquid Phase Properties. *J. Chem. Theory Comput.* **2014**, *10* (8), 2906−2910.

(25) Ho, C.-H.; Valentine, M. L.; Chen, Z.; Xie, H.; Farha, O.; Xiong, W.; Paesani, F. Structure and Thermodynamics of Water Adsorption in NU-1500-Cr. *Commun. Chem.* **2023**, *6* (1), No. 70.

(26) Terranova, Z. L.; Agee, M. M.; Paesani, F. Water Structure and Dynamics in Homochiral [Zn(l-L)(X)] Metal−Organic Frameworks. *J. Phys. Chem. C* **2015**, *119* (32), 18239−18247.

(27) Terranova, Z. L.; Paesani, F. The Effects of Framework Dynamics on the Behavior of Water Adsorbed in the [Zn(l -L)(Cl)] and Co-MOF-74 Metal−Organic Frameworks. *Phys. Chem. Chem. Phys.* **2016**, *18* (11), 8196−8204.

(28) Rieth, A. J.; Hunter, K. M.; Dincă, M.; Paesani, F. Hydrogen Bonding Structure of Confined Water Templated by a Metal-Organic Framework with Open Metal Sites. *Nat. Commun.* **2019**, *10* (1), 4771.

(29) *JOSA* Porto, S. P. S. Angular Dependence and Depolarization Ratio of the Raman Effect. *J. Opt. Soc. Am.* **1966**, *56* (11), 1585−1589.

(30) Bernstein, H. J.; Buckingham, A. D. Resonance Raman Spectra [and Discussion]. *Philos. Trans. R. Soc., A* **1979**, *293* (1402), 287−302.

(31) Chen, T.; Dou, J.-H.; Yang, L.; Sun, C.; Oppenheim, J. J.; Li, J.; Dincă, M. Dimensionality Modulates Electrical Conductivity in Compositionally Constant One-, Two-, and Three-Dimensional Frameworks. *J. Am. Chem. Soc.* **2022**, *144* (12), 5583−5593.

https://doi.org/10.1021/acs.chemmater.4c00172
Chem. Mater. 2024, 36, 3395−3404